Nanorods of ZnO Made by Flame Spray Pyrolysis

Murray J. Height, Lutz Mädler, and Sotiris E. Pratsinis*

Particle Technology Laboratory, Institute of Process Engineering, ETH Zurich, Sonneggstrasse 3, ML F13, CH-8092 Zürich, Switzerland

Frank Krumeich

Laboratory for Inorganic Chemistry, ETH Zurich, Wolfgang-Pauli-Strasse 10, CH-8093 Zürich, Switzerland

Received September 27, 2005. Revised Manuscript Received November 3, 2005

Inorganic nanorods with closely controlled aspect ratio were made by flame spray pyrolysis − a single-step, continuous, and scaleable process. Indium and tin dopants selectively affect a specific ZnO crystal plane and are incorporated into its lattice. Nanorod formation is attributed to the higher valency and coordination of indium and tin dopants relative to zinc and the associated disruption of crystal growth within the Zn plane. In contrast, lithium, with an equivalent ionic radius to these dopants but lower valency than zinc, has no effect on the ZnO texture. The formation of the nanorods within the flame occurs by annealing crystallization during flame cooling.

Introduction

Nanorods are solid structures featuring a dominant one-dimensional nature. While similar in geometry, they are shorter than nanowires, nanofilaments, and nanofibers exhibiting unique electronic, optical, and mechanical properties that appeal to a range of applications in electronics,[1,2] sensors,[3] optical components and displays,[1] polymer-composites,[4] and actuator devices.[5] As a result, there is profound interest in understanding the basic mechanism for nanorod growth. For nanoscale inorganic crystals such as ZnO, the introduction of trace amounts of indium,[6] tin,[7] and other[8] elements can induce preferential growth within specific crystal planes[9] resulting in asymmetric crystals. Nanorod growth may also be controlled through the reactant composition ratio such as the ratio of oxygen to zinc precursor.[10,11] Typically nanorods are made by vapor deposition or wet-chemistry[12] routes that are difficult, however, to scale up, limiting their applications somewhat. Flame synthesis is a technique that can be readily scaled to produce nanostructured materials in high volume at relatively low cost.[13] Flame-generated materials are dominated typically by spherical primary particles and chainlike agglomerates, as shown even recently by in situ synchrotron X-ray scattering.[14]

From a fundamental perspective, the ability to selectively and rapidly form anisotropic structures of flame-made particles in a controlled fashion has been a unique challenge. Carbon nanotubes have been made using flames,[15] but controlled creation of such pronounced linear features of flame-made inorganic materials has not been achieved yet. Short rodlike particles may have been observed in flames before;[16] however, their formation is not controlled or a dominant feature of these products.[17]

Here we report the rapid and direct synthesis of ZnO nanorods with close control of aspect ratio (ratio of length to width) by flame spray pyrolysis (FSP), a combustion-based process whereby a liquid solvent containing appropriate precursors is injected and atomized into a flame.[18] The FSP has been used for synthesis of a variety of noble metal ceramic and mixed ceramic particles for catalyst, sensor, and even dental[19] materials but never before for nanorods. Formation of the nanorods occurs exclusively in the vapor phase giving insight into a wall-free formation mechanism.

* Corresponding author. Fax: +41-1-632-15-95. E-mail: pratsinis@ptl.mavt.ethz.ch.

(1) Xia, Y. N.; Yang, P. D.; Sun, Y. G.; Wu, Y. Y.; Mayers, B.; Gates, B.; Yin, Y. D.; Kim, F.; Yan, Y. Q. *Adv. Mater.* **2003**, *15* (5), 353−389.
(2) Wang, Z. L. *Nanowires and nanobelts: Materials, properties and devices. Metal and semiconductor nanowires*; Kluwer: Norwell, MA, 2003; Vol. 1.
(3) Dai, Z. R.; Pan, Z. W.; Wang, Z. L. *Adv. Funct. Mater.* **2003**, *13* (1), 9−24.
(4) Li, L. M.; Beniash, E.; Zubarev, E. R.; Xiang, W. H.; Rabatic, B. M.; Zhang, G. Z.; Stupp, S. I. *Nat. Mater.* **2003**, *2* (10), 689−694.
(5) Lin, M.; Chang, F. K. *Compos. Sci. Technol.* **2002**, *62* (7−8), 919−939.
(6) Wen, J. G.; Lao, J. Y.; Wang, D. Z.; Kyaw, T. M.; Foo, Y. L.; Ren, Z. F. *Chem. Phys. Lett.* **2003**, *372* (5−6), 717−722.
(7) Gao, P. X.; Ding, Y.; Wang, I. L. *Nano Lett.* **2003**, *3* (9), 1315−1320.
(8) Sun, X. C.; Zhang, H. Z.; Xu, J.; Zhao, Q.; Wang, R. M.; Yu, D. P. *Solid State Commun.* **2004**, *129* (12), 803−807.
(9) Kong, X. Y.; Ding, Y.; Yang, R.; Wang, Z. L. *Science* **2004**, *303* (5662), 1348−1351.
(10) Yan, H. Q.; He, R. R.; Pham, J.; Yang, P. D. *Adv. Mater.* **2003**, *15* (5), 402−405.
(11) Tseng, Y. K.; Hsu, H. C.; Hsieh, W. F.; Liu, K. S.; Chen, I. C. *J. Mater. Res.* **2003**, *18* (12), 2837−2844.
(12) Tian, Z. R. R.; Voigt, J. A.; Liu, J.; McKenzie, B.; McDermott, M. J.; Rodriguez, M. A.; Konishi, H.; Xu, H. F. *Nat. Mater.* **2003**, *2* (12), 821−826.
(13) Mueller, R.; Madler, L.; Pratsinis, S. E. *Chem. Eng. Sci.* **2003**, *58* (10), 1969−1976.
(14) Beaucage, G.; Kammler, H. K.; Mueller, R.; Strobel, R.; Agashe, N.; Pratsinis, S. E.; Narayanan, T. *Nat. Mater.* **2004**, *3* (6), 370−374.
(15) Height, M. J.; Howard, J. B.; Tester, J. W.; Vander Sande, J. B. *Carbon* **2004**, *42* (11), 2295−2307.
(16) Akhtar, M. K.; Pratsinis, S. E.; Mastrangelo, S. V. R. *J. Am. Ceram. Soc.* **1992**, *75* (12), 3408−3416.
(17) Tani, T.; Mädler, L.; Pratsinis, S. E. *J. Nanopart. Res.* **2002**, *4* (4), 337−343.
(18) Mädler, L.; Kammler, H. K.; Mueller, R.; Pratsinis, S. E. *J. Aerosol Sci.* **2002**, *33* (2), 369−389.

10.1021/cm052163y CCC: $33.50
Published on Web 12/23/2005

Experimental Section

The FSP apparatus is described in detail elsewhere.[20] Here, a dispersion gas flow rate of 5 L/min and a pressure drop of 1.5 bar was maintained across the nozzle during FSP operation. Liquid precursor was fed through the nozzle capillary at 5 mL/min using a rate-controlled syringe pump (Inotech R232). A sheath gas flow of 5 L/min of oxygen was issued concentrically around the nozzle to stabilize and contain the spray flame. Peak temperatures for the spray flame are typically in the range of 2000 K to 2500 K as measured nonintrusively by Fourier transform infrared spectrometry.[18] All gas flows (Pan Gas, >99.95%) were metered using mass flow controllers (Bronkhorst). A water-cooled, stainless steel filter housing supported a glassfiber filter (Whatman GF/D; 25.7 cm diameter) for collection of the flame-produced powder with the aid of a vacuum pump (Busch). The basis liquid precursor solution was composed of toluene (Fluka, 99.5%) and zinc naphthenate (STREM Chemicals, 65% in mineral spirits). Dopant species were indium (indium acetyl acetonate; Aldrich, 99.99%), tin (stannous 2-ethyl hexanoate; Aldrich 95%), and lithium (lithium *tert*-butoxide; Aldrich, 1.0 M in tetrahydrofuran). Li-doped ZnO samples were also prepared using lithium acetyl acetonate (Aldrich, 97%), resulting in powders identical to the *tert*-butoxide precursor. Dopant concentrations ranged between 1 and 10 at. % with respect to the Zn metal. The total metal concentration for each precursor solution was 0.5 mol/L. The thermal stability of the powders was investigated by annealing them in ambient air in a Carbolite CWF1300 temperature-programmed oven. Samples were heated at 5 °C/min to either 700 °C or 900 °C, maintained at that temperature for 5 h, followed by cooling at 10 °C/min.

Powders were characterized by X-ray diffraction (XRD) in a Bruker AXS D8 Advance spectrometer at 2θ (Cu Kα) 20−70°, step size of 0.03°, and scan speed of 0.6°/min (source 40 kV, 40 mA). XRD patterns were analyzed using the Fundamental Parameter method to match the profile of individual peaks within each pattern, allowing extraction of crystallite size information.[21] BET adsorption isotherms and specific surface area analysis was performed using a MicroMeritics TriStar 3000 system after degassing in nitrogen for 1.5 h at 150 °C. The specific surface area (SSA) was measured using five-point nitrogen adsorption at 77 K. The BET equivalent diameter was evaluated from the measured SSA for each sample, assuming a spherical primary particle geometry and a composition-corrected density. Transmission electron microscopy analysis was carried out with a Phillips CM30ST microscope (LaB_6 cathode, 300 kV). A confocal Raman microscope (Labram, Jobin Yvon, ex DILOR Instruments SA) was used for the Raman spectra. An internal HeNe laser at 632.8 nm with approximately 2.5 mW power was used for ex situ measurements. Raman spectra were recorded from 200 to 1050 cm^{-1} with a line resolution of 4 cm^{-1}. Raman band positions were calibrated against the spectrum of a neon lamp (Penray, Oriel). With the confocal hole at 500 μm, the spatial resolution was 3−5 μm^3.

Results and Discussion

Figure 1 shows XRD patterns for pure and indium-doped ZnO (1 to 10 at. %). The XRD pattern of pure ZnO (bold line) shows the typical reflections of ZnO with the crystal plane assignments indicated in the upper portion of the frame.

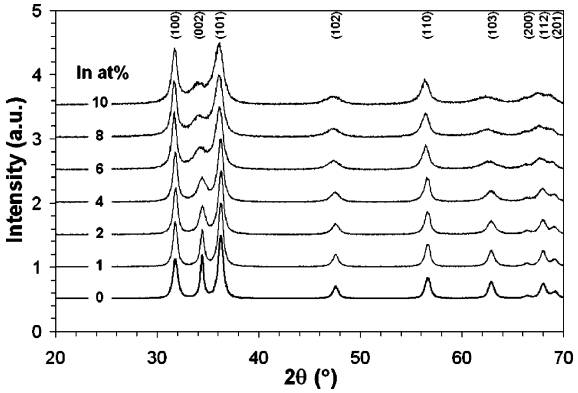

Figure 1. X-ray diffraction patterns for In-doped ZnO (0−10 at. %). Crystal plane indices for each diffraction signal are shown in the upper frame. All patterns are consistent with the hexagonal wurtzite structure. Note the reduction of the (002) peak with increasing dopant concentration.

Patterns for indium-doped ZnO are arranged upward from the pure ZnO pattern with increasing dopant concentration. All patterns are normalized relative to the intensity of the peak corresponding to the (101) crystal plane at 36.3°. The main feature of the patterns is the conservation of the wurtzite lattice structure and the diminishing intensity and broadening of the primary (002) peak as indium dopant concentration is increased. In contrast, the primary (100) and (101) planes remain relatively unaffected. This is consistent with Pacholski et al.[22] and in particular Cheng and Samulski[23] who made ZnO nanorods in ethanol showing also a reduced crystallite size within the (002) plane.

Figure 2a,b,c shows the (100), (002), and (101) peaks in detail (2θ = 28 to 38°) for (a) In-, (b) Sn-, and (c) Li-doped ZnO samples for 1−10 at. % dopant concentration. For both In- and Sn-doped ZnO, the (002) peak exhibits a dramatic reduction in intensity and pronounced broadening with increasing dopant content, in stark contrast with Li-doped ZnO. This is consistent with the crystallite size in the (002) plane becoming smaller, while the crystallite size in the (101) plane appears to remain relatively constant for In- and Sn-doped ZnO. Figure 2d,e,f shows the average crystallite size associated with the (100) and (002) peaks in each XRD pattern as a function of dopant concentration. For the In-doped ZnO, the crystallite size in the (002) plane decreases by a factor of 5 from 27 to 5 nm as indium concentration increases from 0 to 8 at. % (Figure 3d). The crystallite size in the (100) plane increases slightly from 18 to 20 nm before gradually declining to 16 nm. Sn-doped ZnO shows a similar, yet steeper, trend to that of In-doped ZnO, as the crystallite size in the (002) plane decreases from 27 to 6 nm with the addition of only 4 at. % dopant. The corresponding change in crystallite size for the (100) plane is 18 to 14 nm with 4 at. % Sn dopant (similar effect for 8% In-doped ZnO). Both In and Sn selectively reduce the crystallite size in the (002) plane while only slightly decreasing the crystallite size in the (100) plane. In stark contrast, the crystallite sizes for the Li-doped ZnO remain unaffected even for dopant concentrations up to 10 at. %. The SSA increases steadily from 53 to 77 m^2/g as In concentration increases from 0 to 10 at. %

(19) Schulz, H.; Madler, L.; Pratsinis, S. E.; Burtscher, P.; Moszner, N. *Adv. Funct. Mater.* **2005**, *15* (5), 830−837.
(20) Mädler, L.; Stark, W. J.; Pratsinis, S. E. *J. Mater. Res.* **2003**, *18* (1), 115−120.
(21) Cheary, R. W.; Coelho, A. *J. Appl. Crystallogr.* **1992**, *25*, 109−121.
(22) Pacholski, C.; Kornowski, A.; Weller, H. *Angew. Chem., Int. Ed.* **2002**, *41* (7), 1188−1191.
(23) Cheng, B.; Samulski, E. T. *Chem. Commun.* **2004**, *8*, 986−987.

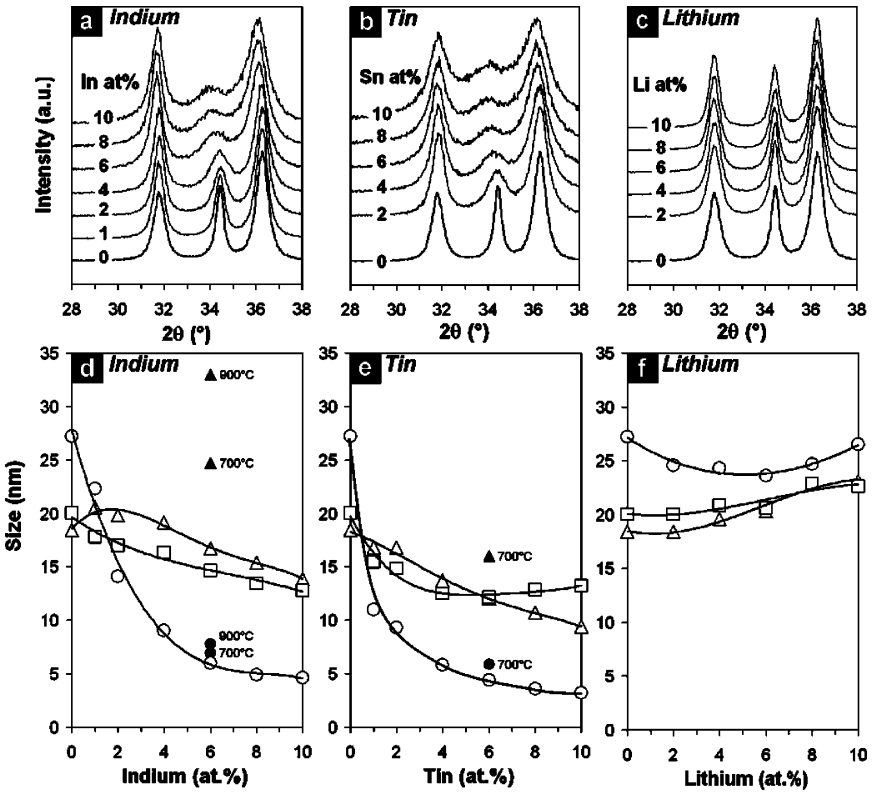

Figure 2. Crystallite size analysis. Panels a, b, and c give detail of XRD patterns for ZnO doped with In, Sn, and Li, respectively. The peaks correspond to the (100), (002), and (101) planes of the wurtzite structure at 31.8°, 34.5°, and 36.3° 2θ, respectively. Panels d−f indicate control of plane-specific ZnO crystallite sizes (△- (100); ○ − (002)) as a function of dopant concentration for (d) In, (e) Sn, and (f) Li, together with the BET equivalent diameter (□) for each of the doped ZnO samples. The Sn-doped ZnO shows a steeper variation than the In-doped ZnO, in agreement with XRD. Annealed samples (filled symbols) and associated temperatures are shown in panels d and e.

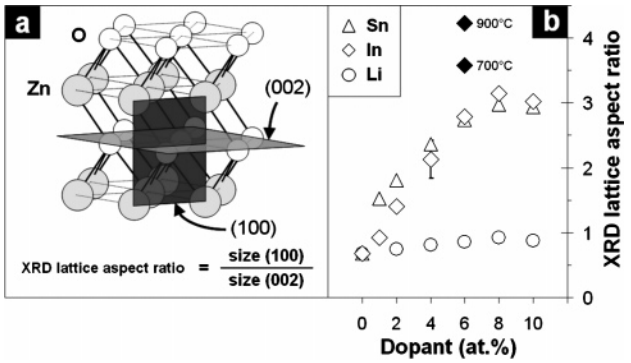

Figure 3. Control of nanorod aspect ratio. Panel a shows the ZnO lattice along with the calculation of XRD lattice aspect ratio from the ratio of (100) to (002) XRD crystallite size measurements. Panel b shows the XRD lattice aspect ratio as a function of dopant concentration for In- (◊), Sn- (△), and Li-doped (○) ZnO and annealed 6 at. % In−ZnO (♦) with the corresponding temperatures.

and from 53 to 85 m^2/g as tin concentration increases from 0 to 6 at. % followed by a decrease to 75 m^2/g at doping up to 10 at. %. The Li-doped ZnO exhibits the same SSA as the pure ZnO (53 m^2/g) for dopant concentrations up to 6 at. % and then decreases to 43 m^2/g at doping up to 10 at. %. The BET equivalent diameter (d_{BET}) for the In-, Sn-, and Li-doped ZnO samples are shown also as a function of dopant concentration in Figure 2d,e,f (squares). The thermal stability of the In-doped nanorods was investigated by annealing in air for 5 h at either 900 or 700 °C (Figure 2d). At both temperatures, the XRD crystallite size in the (100) and (002) planes of the pure ZnO powders increased dramatically from 23 ± 5 nm (as prepared) to 65 ± 2 nm for 700 °C and 133 ± 2 nm for 900 °C. For the 6 at. % In-doped ZnO samples, the crystallite size in the (100) plane increased from the as-prepared value of 16.7 nm to 24.7 nm (700 °C) and 33.0 nm (900 °C) (Figure 2d). In contrast, the crystallite size in the (002) plane remained relatively close to the as-prepared value of 6.0 nm, increasing to 6.9 nm (700 °C) and 7.8 nm (900 °C). The 6 at. % Sn-doped ZnO samples showed a similar increase in the crystallite size in the (100) plane from 12.1 nm (as prepared) to 16.0 nm (700 °C) and the crystallite size in the (002) plane changed from 4.4 (as-prepared) to 5.9 nm (700 °C) (Figure 2e). Furthermore, for annealing at 900 °C the crystallite size in both (100) and (002) planes increased dramatically to 98.1 and 35.3 nm, respectively, (not shown in Figure 2e).

Zinc oxide has a hexagonal-close-packed wurtzite structure in which the crystal is composed of alternating planes of Zn and O atoms (Figure 3a). The (002) plane lies in parallel to the O and Zn planes while the (100) plane lies perpendicular to the (002) plane, intersecting alternating layers of Zn and O. The crystallite size in the (002) and (100) planes can essentially be considered as metrics of 'diameter' (D) and 'length' (L), respectively (Figure 3a). The crystal aspect ratio (L/D) can therefore be estimated by the ratio of the crystallite sizes in the (100) and (002) planes, designated here as the XRD lattice aspect ratio. Figure 3b shows the variation of XRD lattice aspect ratio with dopant concentration for the In-, Sn-, and Li-doped ZnO as calculated from the crystallite size measurements. For the In-doped ZnO the XRD lattice aspect ratio increases steadily by a factor of 5 from 0.6 to 3.1 as dopant concentration is increased from 0 to 10 at. %.

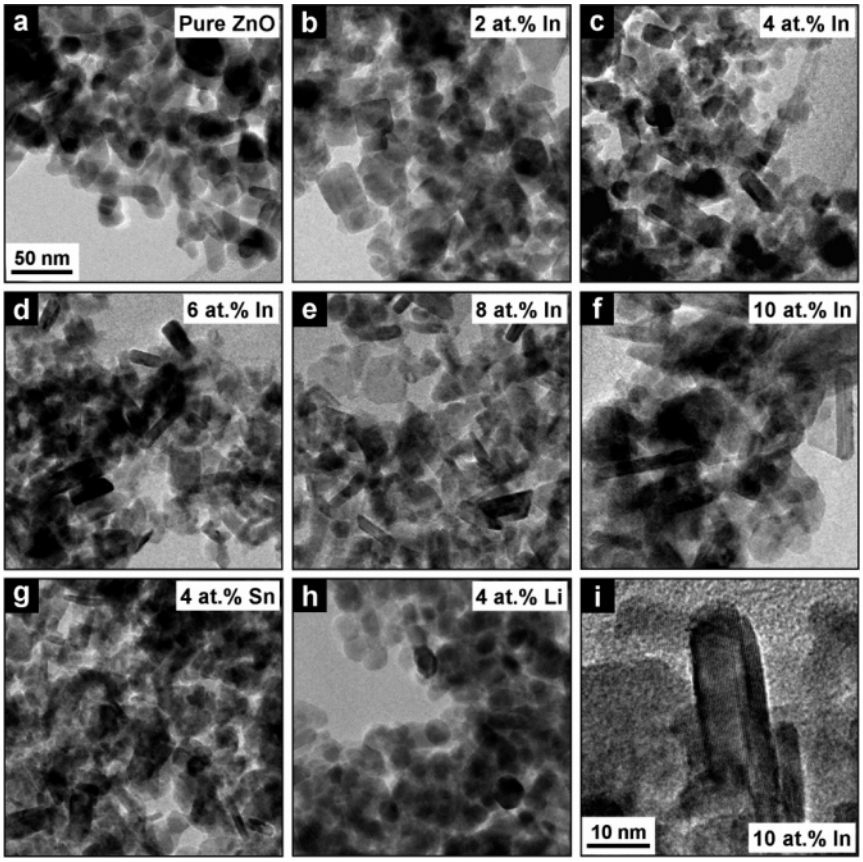

Figure 4. Nanorod and nanoparticle images: (a) pure ZnO also showing the scale marker for all images except for image i, (b−f) 2−10 at. % In-doped ZnO and 4 at. %, (g) Sn-doped ZnO, and (h) Li-doped ZnO. The crystal morphology of the In-doped ZnO clearly changes from spheroidal (pure ZnO), to cuboid, and to increasingly rodlike as In concentration increases, consistent with XRD (Figure 2a,d). Image i shows a high-resolution TEM of a single 10 at. % In-doped ZnO nanorod crystal.

Similarly, the Sn-doped ZnO also increases in XRD lattice aspect ratio as more dopant is added; however, tin appears to have a stronger influence than indium at lower dopant concentrations. The XRD lattice aspect ratio of the Li-doped ZnO remains essentially the same as pure ZnO as that concentration is increased up to 10 at. %. The annealed pure ZnO samples showed a dramatic jump in crystallite size in both the (100) and (002) planes upon annealing, giving an XRD lattice aspect ratio of unity for both temperatures. The In-doped ZnO samples showed a selective increase in crystallite size in the (100) plane, yielding an increase in XRD lattice aspect ratio from 2.8 (as-prepared) to 3.6 (700 °C) and 4.2 (900 °C) (Figure 3b). For Sn-doped ZnO the XRD lattice aspect ratio remained constant at 2.7 (for 700 °C) and a had slight increase to 2.8 (for 900 °C); however, this was also associated with a resultant particle size similar to that of the annealed pure ZnO, consistent with the tin dopant leaving the ZnO lattice at higher annealing temperatures (Figure 2e). This is in contrast to indium where the XRD lattice aspect ratio is dramatically enhanced for the two annealing temperatures considered here.

Figure 4 shows a series of TEM images for (a) pure ZnO along with (b−h) 2−10 at. % In-doped ZnO. Pure ZnO contains mainly spheroidal particles typically with diameters of 20 nm with occasional rodlike structures, consistent with Tani et al.[17] These short, rodlike features seen among the mainly spheroidal particles may arise from a slight oxygen deficiency, in-line with size effects caused by oxygen stoichiometry variation.[10,11] The 2 at. % In-doped ZnO (b) shows particles with cuboid morphology, while for 4 at. % doping (c) the particles begin to exhibit an elongated morphology. Between 6, 8, and 10 at. % (d, e, and f) the particles exhibit increasing rodlike appearance. The 10 at. % In-doped ZnO sample (f) in particular is dominated by nanorod features with diameters between 10 and 20 nm and lengths up to about 100 nm. The XRD measurements (Figure 3), showing an increased XRD lattice aspect ratio with dopant concentration, are consistent with these TEM images.

Figure 4c,g,h images also demonstrate the influence of the 4 at. % dopant concentration for the In-, Sn-, and Li-doped ZnO. Compared to pure ZnO (a), the In- (c) and Sn-doped ZnO (g) exhibit rodlike structures. Note that these pictures are essentially a cross-sectional view of a sample that possesses random alignment. Thus, the pictures show only a limited aspect of the true geometry. Rodlike features aligned parallel to the image plane, however, are clearly evident in these images. Li-doped ZnO (h) is dominated by spheroidal particles similar to pure ZnO (a). Figure 4i shows a high-resolution TEM image of an individual nanorod with the single-crystalline morphology of each structure clearly evident.

Figure 4 reveals nanorods with aspect ratios between 5 and 10 while the XRD lattice aspect ratios are all less than 4. This difference may result from differences in the averaging of the characterization methods. The TEM images give a representation of the sample essentially in terms of

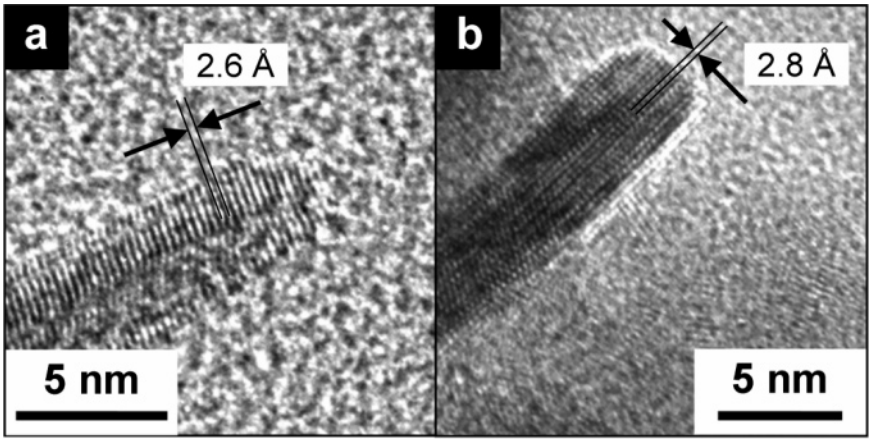

Figure 5. High-resolution TEM images of In-doped ZnO (10 at. %) nanorods. Lattice planes for (a) cross-sectional and (b) axial directions of nanorod crystals are shown. The measured spacings are consistent with the (002) (ca. 2.6 Å; a) and (100) (ca. 2.8 Å; b) planes, respectively, confirming the nanorod length along the *c*-axis.

number while the XRD gives averages according to mass. The characterization methods therefore sample different moments of the particle size distribution and the resulting averages are expected to differ, an effect that is exacerbated here with nonspherical particles. The key point, however, is that together the methods give a consistent picture of the aspect ratio trend to increase with indium or tin dopant level and the more drastic aspect ratio change for tin than for indium at low dopant concentrations. There are two main questions regarding nanorod formation: First, how do the dopants induce the growth of nanorods? Second, how do nanorods form in the flame? The XRD patterns for each of In-, Sn-, and Li-doped ZnO samples exhibit the same characteristic pattern with pure ZnO having a wurtzite crystal structure (Figures 1 and 2). For the dopant levels considered in this study there were no additional XRD peaks associated with the dopant oxides, indicating no new crystal-phase formation. The structural agreement between the doped and pure ZnO patterns indicates that each of the dopant atoms do not significantly alter the packing structure of the parent ZnO lattice. The elemental composition of the nanorods was identical to the composition of the liquid precursor solution as confirmed by energy-dispersive X-ray spectroscopy in the present study and is consistent with other FSP-made powders.[24]

Although the dopants are incorporated within the wurtzite lattice, the lattice geometry is altered for higher indium (Figure 2a) and tin (Figure 2b) concentrations with respect to the 2θ position of the (002) peak. Comparing the relative displacement of the maxima of the (100) and (002) peaks relative to the position of the (101) peak, treated here as an internal reference, it is possible to gain an insight of the distortion in crystal geometry. For dopant concentrations up to 6 at. %, the (100) and (002) peaks remain at positions identical to those of pure ZnO. However, for dopant concentrations of 8 and 10 at. %, the maximum of the (002) peak shifts toward higher interplanar *d* spacing (smaller 2θ) values while the (100) peak remains at the same *d* spacing. This peak shift is noticeable only for higher dopant concentrations, the specificity of the shift to the (002) peak is consistent with the dopant atoms being incorporated within the cross-sectional plane.

Figure 5 shows high-resolution TEM images of 10 at. % In-doped ZnO nanorod crystals. The approximate spacing between the lattice planes in the cross-sectional and axial directions are consistent with the (002) and (100) planes, respectively. The incorporated dopants may influence the surrounding lattice either by their size, valency, or degree of coordination. The ionic radii, based on a coordination number of 6, of In (0.80 Å), Sn (0.69 Å), and Li (0.76 Å) are very similar[25] to that of Zn (0.74 Å), so dopant atom size is unlikely to induce the observed rodlike geometry. Similar dopant sizes can create a substitutional defect as with Sn and Al doping[26] on TiO_2. The peak shift described in the above paragraph is most pronounced for indium, the dopant species with the largest ionic radius relative to zinc, and even then the shift occurs only at high dopant concentrations where the dopant size is likely to increase the *d* spacing for the (002) planes. While size is not a distinguishing factor between the dopants, their valencies are quite different than zinc (+2): with Li of lower valency (+1), and In and Sn each of higher valency (+3 and +4, respectively).

Multivalent dopants have also been reported to influence the morphology of other crystals such as calcium oxide monohydrate.[27] Here, the higher valency of In and Sn relative to Zn would lead to greater coordination with surrounding O than for Zn atoms within the same crystal plane. The In and Sn atoms therefore could have a disrupting influence, hindering crystal growth within the Zn layer.[9] This hindering effect is observed in the decreasing crystallite size in the (002) plane as the In and Sn dopant concentration is increased (Figure 2). The more pronounced nanorod-forming influence of Sn relative to In at low dopant concentrations may be attributed also to higher Sn valency and thus larger disruptive influence. Conversely, the lower valency of Li means that this atom would have minimal disruptive influence within

(24) Stark, W. J.; Maciejewski, M.; Mädler, L.; Pratsinis, S. E.; Baiker, A. *J. Catal.* **2003**, *220* (1), 35−43.

(25) Shannon, R. D. *Acta Crystallogr.* **1976**, *A32*, 751−767.

(26) Akhtar, M. K.; Pratsinis, S. E.; Mastrangelo, S. V. R. *J. Mater. Res.* **1994**, *9* (5), 1241−1249.

(27) Touryan, L. A.; Lochhead, M. J.; Marquardt, B. J.; Vogel, V. *Nat. Mater.* **2004**, *3* (4), 239−243.

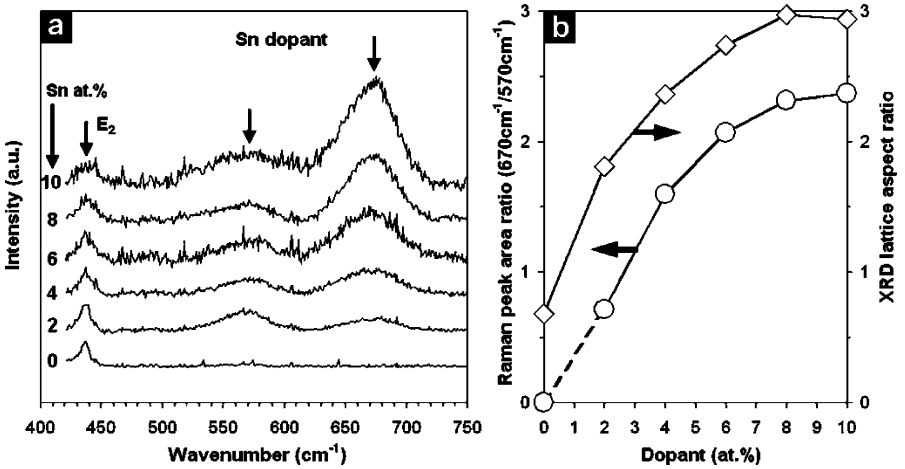

Figure 6. Raman spectroscopy of Sn-doped ZnO nanorods: (a) spectra (632 nm excitation) at different dopant contents. The peaks at 570 and 670 cm^{-1} are associated with different coordination states of the Sn dopant. The latter peak reflects higher coordination. (b) The ratio of areas (○) below the peak at 670 cm^{-1} to that below 570 cm^{-1} is consistent with the XRD lattice aspect ratio (◊) (Figure 3b).

the Zn plane, giving the observed invariance of the crystallite size in the (002) plane (Figure 2f).

Figure 6a shows Raman spectra for 0−10 at. % Sn-doped ZnO. Each spectrum was normalized to the amplitude of the E_2 mode (437 cm^{-1}) of the wurtzite. All Sn-doped powders exhibit two additional peaks at 570 and 670 cm^{-1}. These peaks are indicative of vibrations associated with the tin dopant atoms within the crystal, while the peak at 670 cm^{-1} is associated with a more highly coordinated structure than that of the 570 cm^{-1} peak.[28] Figure 6b shows the ratio (diamonds) of areas below the 670 cm^{-1} peak to that below the 570 cm^{-1} peak as a function of dopant concentration. The increasing proportion of highly coordinated dopant, as indicated by that ratio, correlates well with the XRD lattice aspect ratio (circles) trend (Figure 3b), further supporting the effect of dopants on the crystal geometry.

The FSP delivers liquid precursors to a high temperature where they vaporize, oxidize, and subsequently form metal-oxide clusters that coagulate into nanometer-scale particles. Particle growth can continue via surface reactions and collisions with other particles.[18] Precursor reaction and particle formation occur in the vapor phase; therefore, the initial stage of the nanorod formation process is the formation of primary particles from the vapor. In the early stages of the flame, particles are at a higher temperature than the melting point of ZnO (1970 °C), and so they would be spherical in shape and liquidlike. However, in the latter region of the flame, particles cool rapidly, solidify, and crystallize.

The dopants could influence particle formation and morphology in two regions of the flame: First, during the initial flame stages, the dopant presence may affect the primary particle size by influencing the initial cluster formation, sintering, and growth rate. Second, during the late flame stages when gas temperature decreases significantly and particles crystallize,[29] dopants within the particles may begin to influence the formation of the crystal structure as described previously, disrupting growth in the (002) plane. The final nanorod shapes therefore could be attributed to particle annealing and rearrangement during the later stages of the flame. An alternative mechanism based on epitaxial growth of the nanorods via selective surface growth of the alternating Zn and O planes could have been possible, similar somewhat to that of carbon nanotube formation.[15] The thermal stability analysis for the In- and Sn-doped powders indicates that while dopants incorporated in the structure of the ZnO lattice influence particle geometry, the nanorod formation in the flame is likely to be a tradeoff between solubility of the dopants within the lattice (rapid flame cooling may give locally higher dopant concentrations in the lattice) and structural rearrangement to give the final nanorod structure (enhanced by maintaining a prolonged high temperature). The observed short rod lengths (<100 nm) and the absence of reactor wall surfaces during nanorod synthesis indicates that growth proceeds exclusively by gas-phase processes, in contrast to vapor condensation methods.[6,11] The formation of these structures in the gas phase makes FSP an appealing process for continuous and scaleable synthesis of nanorods.

Conclusions

Flame synthesis of inorganic nanorods with closely controlled aspect ratio has been demonstrated, probably for the first time. Zinc oxide doped with In, Sn, or Li up to 10 at. % exhibited a single-phase wurtzite structure. In and Sn dopants, however, alter progressively the shape of the ZnO particles to a rodlike shape with increasing dopant concentration. Sn has a stronger nanorod-forming influence than In at low dopant levels. Lithium does not influence the shape of the ZnO. The XRD lattice aspect ratio for both the In- and Sn-doped ZnO crystals was increased by a factor of 5 as dopant content increased up to 10 at. % and was confirmed by TEM. The specific surface area for In- and Sn-doped ZnO increased with dopant concentration, with Sn giving a steeper increase, consistent with XRD indicating that for equivalent dopant concentration Sn gives a stronger nanorod-forming effect at lower loading than In. Dopant species selectively affect the (002) plane and are incorporated into the Zn lattice planes. The driving force of nanorod formation with In and Sn as dopants is attributed to their higher valency and coordination relative to zinc and the associated disruption of crystal growth within the Zn plane. In contrast, lithium

(28) Porotnikov, N. V.; Savenko, V. G.; Sidorova, O. V. *Russ. J. Inorg. Chem.* **1983**, *28* (7), 932−934.
(29) Pratsinis, S. E. *Progr. Energy Combust. Sci.* **1998**, *24* (3), 197−219.

with an equivalent ionic radius but lower valency than zinc has no effect on the ZnO texture. The formation of the nanorods within the flame occurs by annealing crystallization during flame cooling, with the final nanorod aspect ratio determined by dopant concentration.

Acknowledgment. We express gratitude to Mr. Laurence Hardwick from the Paul Scherrer Institute for assistance with Raman spectroscopy measurement and analysis.

CM052163Y